Atmospheric Factors Governing Banded Orographic Convection

DANIEL J. KIRSHBAUM

National Center for Atmospheric Research, Boulder, Colorado

DALE R. DURRAN

Department of Atmospheric Sciences, University of Washington, Seattle, Washington

(Manuscript received 25 October 2004, in final form 26 March 2005)

ABSTRACT

The three-dimensional structure of shallow orographic convection is investigated through simulations performed with a cloud-resolving numerical model. In moist flows that overcome a given topographic barrier to form statically unstable cap clouds, the organization of the convection depends on both the atmospheric structure and the mechanism by which the convection is initiated. Convection initiated by background thermal fluctuations embedded in the flow over a smooth mountain (without any small-scale topographic features) tends to be cellular and disorganized except that shear-parallel bands may form in flows with strong unidirectional vertical shear. The development of well-organized bands is favored when there is weak static instability inside the cloud and when the dry air surrounding the cloud is strongly stable. These bands move with the flow and distribute their cumulative precipitation evenly over the mountain upslope.

Similar shear-parallel bands also develop in flows where convection is initiated by small-scale topographic noise superimposed onto the main mountain profile, but in this case stronger circulations are also triggered that create stationary rainbands parallel to the low-level flow. This second dominant mode, which is less sensitive to the atmospheric structure and the strength of forcing, is triggered by lee waves that form over small-scale topographic bumps near the upstream edge of the main orographic cloud. Due to their stationarity, these flow-parallel bands can produce locally heavy precipitation amounts.

1. Introduction

Convective precipitation over shallow orographic terrain often takes the form of quasi-stationary bands. In addition to representing a unique pattern of convective organization, these bands sometimes produce large precipitation enhancements over localized areas. Yoshizaki et al. (2000) studied a case of convective orographic precipitation over the western Kyushu region of Japan in which quasi-stationary rainbands formed downstream of low (400–600 m) topographic obstacles. One rainband in the lee of the Nagasaki Peninsula was remarkably steady, persisting for nearly 24 h and producing between 10 and 30 cm of localized precipitation. Convective orographic rainbands were also observed by Miniscloux et al. (2001) over the Cévennes region of France. Unlike the bands in Kyushu, these bands did not dominate the entire precipitation signature, but were embedded within larger-scale rainfall patterns. After removing the portion of the total precipitation field associated with propagating mesoscale disturbances, a smaller "static" component remained that appeared to be linked to the underlying topography. This static component was characterized by quasi-stationary rainbands that enhanced local precipitation accumulations by up to 10 cm day^{-1}.

Further evidence of quasi-stationary orographic rainbands was provided by Kirshbaum and Durran (2005), who investigated three cases of shallow orographic convection over the Coastal Range in western Oregon. In the best-organized case, rainbands developed over the windward slopes of the Coastal Range that appeared to be more coherent and steadier than those studied by Yoshizaki et al. (2000) and Miniscloux et al. (2001). By contrast, the other two cases had varying degrees of convective organization. The difference between the

Corresponding author address: Daniel J. Kirshbaum NCAR/MMM, P.O. Box 3000, Boulder, CO 80307-3000.
E-mail: kirshbau@ucar.edu

more banded and cellular events appeared to depend on properties of the upstream flow, in particular the low-level vertical wind shear and stability. Numerical simulations of these cases, performed using a highly simplified representation of the Coastal Range topography, qualitatively reproduced the observed banded structures. The simulated rainbands were characterized by roll-like circulations that were roughly parallel to both the mean wind and the shear vectors across the cloud layer.

Although the formation of orographic rainbands appears to depend sensitively on atmospheric parameters, the exact factors that organize the bands are not well understood. For example, while Kirshbaum and Durran (2004, 2005) and Yoshizaki et al. (2000) cite vertical shear as an influential factor in banded events, the idealized experiments of Cosma et al. (2002), which used uniform upstream wind profiles, suggest that flow-parallel bands can form even in the absence of shear. In addition, some ambiguity exists as to whether the mean wind vector or the shear vector over the depth of the unstable cloud layer controls the alignment of orographic rainbands. The rainbands over western Kyushu appeared to be roughly shear parallel (Yoshizaki et al. 2000), while those in Cévennes were organized parallel to the low-level wind (Miniscloux et al. 2001), and those in Oregon were parallel to both the mean wind and shear vectors over the cloud layer (Kirshbaum and Durran 2005).

Some of the differences in the behavior of orographic rainbands may be due to the nature of the features that initiate the convection. The bands in the idealized simulations of Cosma et al. (2002) were forced by tall, though small-horizontal-scale peaks on the elevated terrain, whose patterns of upslope ascent, flow deflection, and leeside convergence formed stationary bands parallel to the flow. Convection in the quasi-idealized simulations of Kirshbaum and Durran (2005), however, was triggered by both a random field of 0.1-K rms thermal noise and by roughness elements on the mountainous topography—whose 30-m rms amplitude are much smaller than the 1.2-km-high peaks considered by Cosma et al. Despite the low rms amplitude of the topographic noise field, flows over the roughened topography produced rainbands that were well defined and stationary. Convection initiated by thermal inhomogeneities in the flow tended to be comparatively disorganized and cellular, though under some atmospheric conditions it also organized into elongated bands.

The goal of this paper is to determine the atmospheric factors that favor the development of banded orographic convection through numerical simulation. Although other factors, such as the geometry of the topographic barrier, may also influence the structure of orographic convection, we limit the range of parameter space under consideration by using the same basic topographic profile for all numerical simulations. The cloud-resolving model and design of the simulations are discussed in the next section. Section 3 describes two mechanisms by which orographic bands may be initiated and illustrates the structure and propagation characteristics of the banded features. The atmospheric parameters controlling band organization are evaluated in section 4, and section 5 contains the conclusions.

2. Numerical simulations

The simulations are performed using the cloud-resolving, nonhydrostatic, and fully nonlinear mesoscale model described in Durran and Klemp (1983) and Epifanio and Durran (2001). This model contains a flux-limited scalar advection scheme (Leveque 1996), a subgrid-scale turbulence formulation (Lilly 1962), and a Kessler warm-rain microphysical parameterization. Ice processes are neglected for simplicity and because the cloud tops in these simulations generally do not extend far above the freezing level. The lower boundary condition is free slip so that the flows impinging upon the mountain can be explicitly specified without the modifications caused by surface momentum, heat, and moisture fluxes. Rotational effects are neglected because of the large characteristic Rossby numbers associated with cross-barrier flow over the narrow topographic profile considered here. This idealized topography, an elongated ridge representative of the northernmost section of the Oregon Coastal Range (see Fig. 1 of Kirshbaum and Durran 2005) over which quasi-stationary rainbands are commonly observed, is given by

$$h(x, y) = \begin{cases} \dfrac{h_0}{16}[1 + \cos(\pi r)]^4, & r \le 1 \\ 0, & \text{otherwise} \end{cases}, \qquad (1)$$

where

$$r^2 = \begin{cases} \left(\dfrac{x - x_0}{4a}\right)^2 + \left(\dfrac{|y - y_0| - B}{4b}\right)^2, & |y - y_0| > B \\ \left(\dfrac{x - x_0}{4a}\right)^2, & \text{otherwise} \end{cases}. \qquad (2)$$

In the preceding, $x_0 = y_0 = 225$ km, $h_0 = 1$ km, $a = 15$ km on the windward side of the mountain and 10 km on the lee, $b = 10$ km, and $B = 30$ km. The relatively modest height of this ridge is roughly similar to that of other mountain ranges associated with shallow convec-

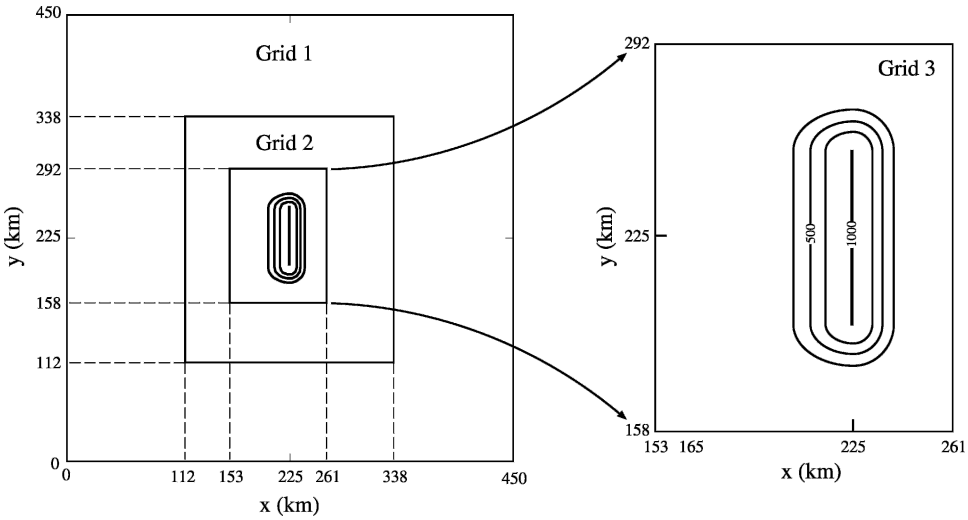

FIG. 1. Numerical domain for quasi-idealized simulations showing the grid nesting and contours of the topography at 250-m intervals.

tive rainbands, including the Cévennes region of France (Miniscloux et al. 2001) and the Koshikijima Islands and Nagasaki Peninsula of Japan (Yoshizaki et al. 2000). In addition to its qualitative similarities with the Coastal Range, the finite extent of the topography in (1) and (2) provides a more accurate representation of upstream blocking effects than that which would be produced by a more simple barrier like an infinitely long 2D ridge.

To provide high spatial resolution directly over the mountain while limiting the overall computational expense, three-level, two-way grid nesting is employed. Figure 1 illustrates the grid configurations and terrain profile for these simulations in which the outermost domain has dimensions of 450 km × 450 km, horizontal grid spacings of 4.5 km, and an integration time step (Δt) of 36 s. Horizontal grid spacings are reduced to 1.5 km and 500 m on the two successively finer nested grids, with respective values of Δt reduced to 12 and 4 s. The vertical resolution (Δz) is 100 m over $0 \leq z < 5$ km, stretching linearly to 400 m over $5 \leq z < 8$ km, then remaining constant at 400 m to the top of the domain at 10 km.

Upstream soundings

The idealized sounding profiles created for this investigation are loosely based on the observed soundings from Kirshbaum and Durran (2005) and are representative of actual upstream conditions during shallow orographic convection events over the Coastal Range. These profiles have constant relative humidity (90%), a two-layer stability structure with constant Brunt–Väisälä frequencies (N_1 below, N_2 above) separated by an interface at $z = 2.5$ km, and cross-barrier wind speeds U that are constant or linearly varying with height. A reference sounding with a surface temperature (T_s) of 285 K, $N_1 = 0.01\ \text{s}^{-1}$, and $N_2 = 0.012\ \text{s}^{-1}$ will henceforth be termed the control (CTRL) case. The θ_e profile for this sounding, which is shown in Fig. 2 along with three other profiles to be discussed in section 4c, decreases from the surface up to $z = 2.5$ km, indicating potential instability in the lower layer. The U velocity increases linearly from $5\ \text{m s}^{-1}$ at the surface to $20\ \text{m s}^{-1}$ at $z = 5$ km, then remains constant to the top of the domain.

3. Initiating bands within the cap cloud

For statically unstable orographic cap clouds to develop obvious convective circulations over realistic time scales, significant energy must be projected into submountain-scale convective modes. This small-scale energy is provided in our numerical simulations by background thermal fluctuations embedded in the flow and small-scale irregularities on the mountainous topography, both of which are initialized using a similar procedure to that described in Kirshbaum and Durran (2005). For the topographic roughness, a uniformly distributed random number is first assigned to each grid point over the mountainous surface, then filtered 12 times by a diffusion operator along each coordinate axis to minimize the forcing at small scales, then scaled to have a specified root-mean-squared (rms) amplitude, nominally selected to be 30 m. A three-dimensional

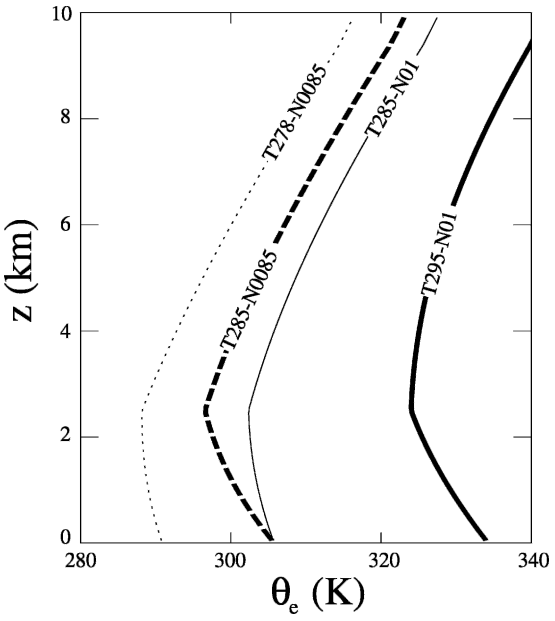

FIG. 2. Equivalent potential temperature (θ_e) profiles of four different thermodynamic soundings considered in this study. Solid thin line is CTRL or T285-N01 sounding (T_s = 285 K, N_1 = 0.01 s^{-1}), dotted thin line is T278-N0085 sounding (T_s = 278 K, N_1 = 0.0085 s^{-1}), solid thick line is T295-N01 sounding (T_s = 295 K, N_1 = 0.01 s^{-1}), and thick dashed line is T285-N0085 sounding (T_s = 285 K, N_1 = 0.0085).

version of this same procedure is followed to add a pattern of 0.1-K rms thermal noise to the initial θ field over the finest numerical grid (grid 3 in Fig. 1). The field of thermal perturbations, which travels downstream with the prevailing flow, is continually replenished by adding random noise to the θ field at the grid's upstream boundaries at each time step.

a. Control simulations

An example of the convective structures generated by these different small-scale forcing mechanisms is provided by two simulations (CTRL-t0.1 and CTRL-h30) that are performed using the grid configuration and mountain profile shown in Fig. 1 and the control sounding described in section 2b. These simulations are identical except for the presence of small-scale thermal fluctuations in the former and roughened topography in the latter. Horizontal cross sections of the cloud liquid water (q_c) fields at z = 1.5 km and t = 3 h for the CTRL-t0.1 simulation (Fig. 3b) and the CTRL-h30 simulation (Fig. 4b) show that, despite their different initiation mechanisms, in both cases the convection over the mountain upslope assumes a clearly banded structure. The topographically initiated bands in Fig. 4b, however, exhibit slightly greater elongation, spacing, and overall organization than the thermally initiated bands in Fig. 3b.

The vertical structures of the rainbands in these control simulations are revealed by the cross sections of q_c and velocity in Fig. 5. Flow-parallel vertical slices along the center of band A (Fig. 3b) at y = 224 km and band B (Fig. 4b) at y = 237 km, which are plotted in Figs. 5a and 5c, show relatively uniform cloud fields along each band. Arrows representing the u and w velocity vectors in the same vertical cross section indicate that the bands form in updrafts over the windward slope and are dissipated in the descending leeside flow. Figures 5b and 5d show cross sections of q_c at x = 220 km and the projection of the velocity vector into the y–z plane. Cloud bands form in the ascending branches of the roll-type circulations, with unsaturated regions in the downdrafts. The convection in the CTRL-h30 case (Fig. 5d) is slightly deeper and more vigorous than that in the CTRL-t0.1 case (Fig. 5b), suggesting that the level of convective excitation from the 30-m rms topographic noise field is greater than that from the 0.1-K rms background thermal noise field.

Although the rainbands forced by thermal fluctuations and topographic roughness in Figs. 3b, 4b, and 5 display some similarities in instantaneous structure, they differ greatly in their propagation and distribution of precipitation. This follows directly from the differences between the two convective initiation mechanisms: background thermal fluctuations in the CTRL-t0.1 case represent a time-dependent forcing that propagates with the flow, while the forcing from the topographic roughness field in the CTRL-h30 case is stationary. As a result, the bands in the CTRL-t0.1 simulation form in ever-changing locations over the upslope and advect downstream, whereas the bands in the CTRL-h30 case are quasi stationary and deposit the bulk of their rainfall over preferred locations. The differences in convective propagation between these two cases cause strong differences in the cumulative surface precipitation at t = 4 h in Fig. 6. The quasi-stationary bands in the CTRL-h30 simulation produce a more banded precipitation distribution (Fig. 6b) with much larger localized accumulations than the transient bands in the CTRL-t0.1 case, which distribute precipitation more evenly over the mountain (Fig. 6a). Maximum precipitation amounts are nearly tripled in the presence of topographic roughness, increasing from 8 mm in the CTRL-t0.1 case to 22 mm in the CTRL-h30 case.

The combined effects of background thermal fluctuations and topographic roughness are considered by a simulation (CTRL-h30-t0.1) that is identical to the other control simulations except for the presence of both small-scale initiation mechanisms. The q_c field at

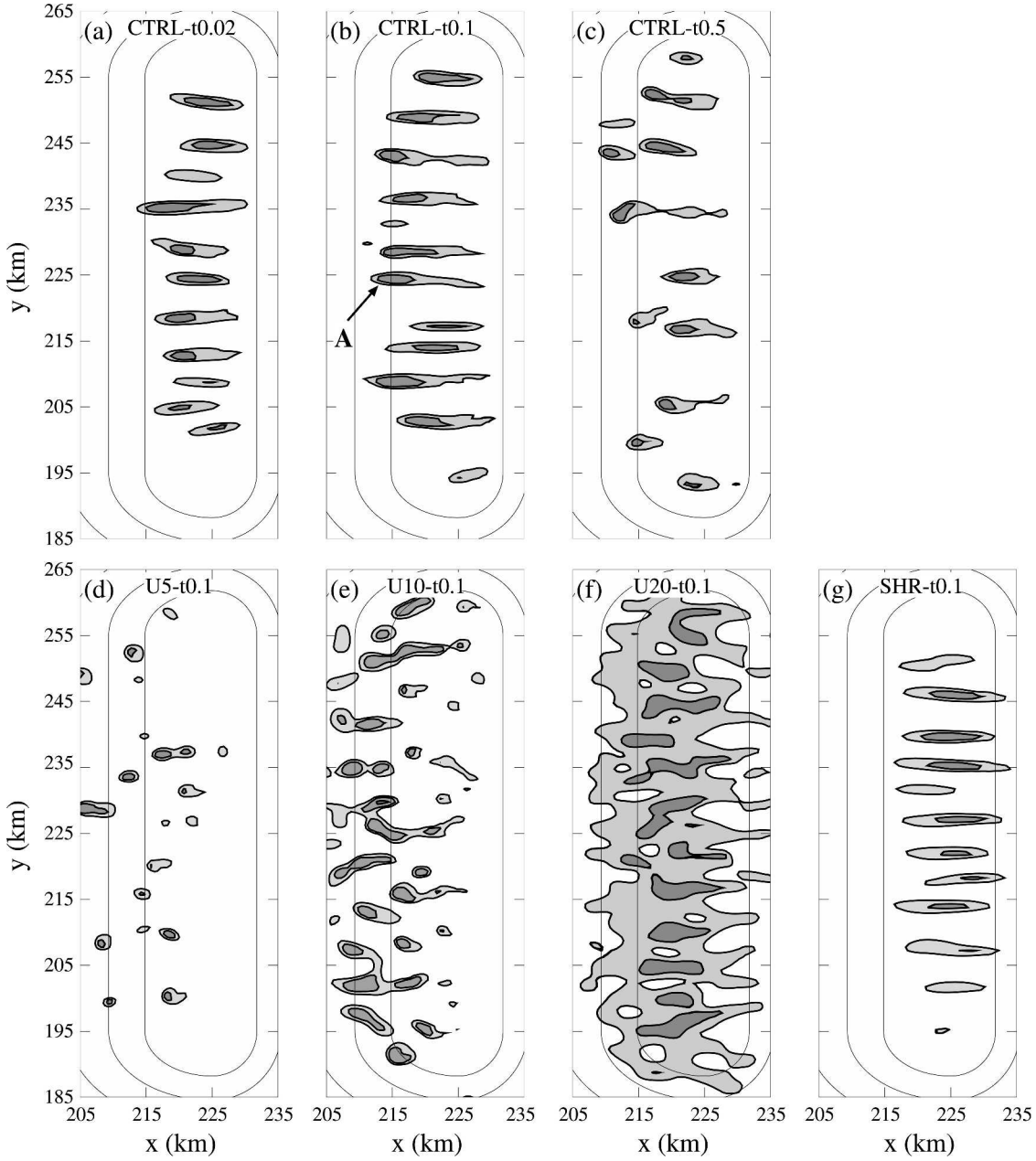

FIG. 3. Cloud liquid water (q_c) fields of simulations with small-scale 0.1-K rms thermal initiation over a smooth mountain at $z = 1.5$ km and $t = 3$ h for (a) CTRL-t0.02, (b) CTRL-t0.1, (c) CTRL-t0.5, (d) U5-t0.1, (e) U10-t0.1, (f) U20-t0.1, and (g) SHR-t0.1 simulations. Contours of q_c are 4 and 8×10^{-4} kg kg^{-1}. Topographic contour interval is 250 m.

$z = 1.5$ km and $t = 3$ h of this simulation is shown in Fig. 7a, indicating that the convective bands are qualitatively similar to those in both the CTRL-t0.1 (Fig. 3b) and CTRL-h30 (Fig. 4b) simulations, though slightly less organized. The overall convective pattern more resembles the CTRL-h30 case, which indicates that the quasi-stationary bands initiated by the topographic roughness elements dominate the more transient features produced by the propagating thermal noise field. This example reflects the basic behavior of simulated flows containing both background thermal fluctuations and topographic roughness: the convection tends to be a mixture of the responses to the two initiation mechanisms and is best organized when both mechanisms acting alone produce similar banded formations that, when combined, have the potential to reinforce each other. As in the CTRL-h30 case, most of the bands in the CTRL-h30-t0.1 simulation are quasi stationary,

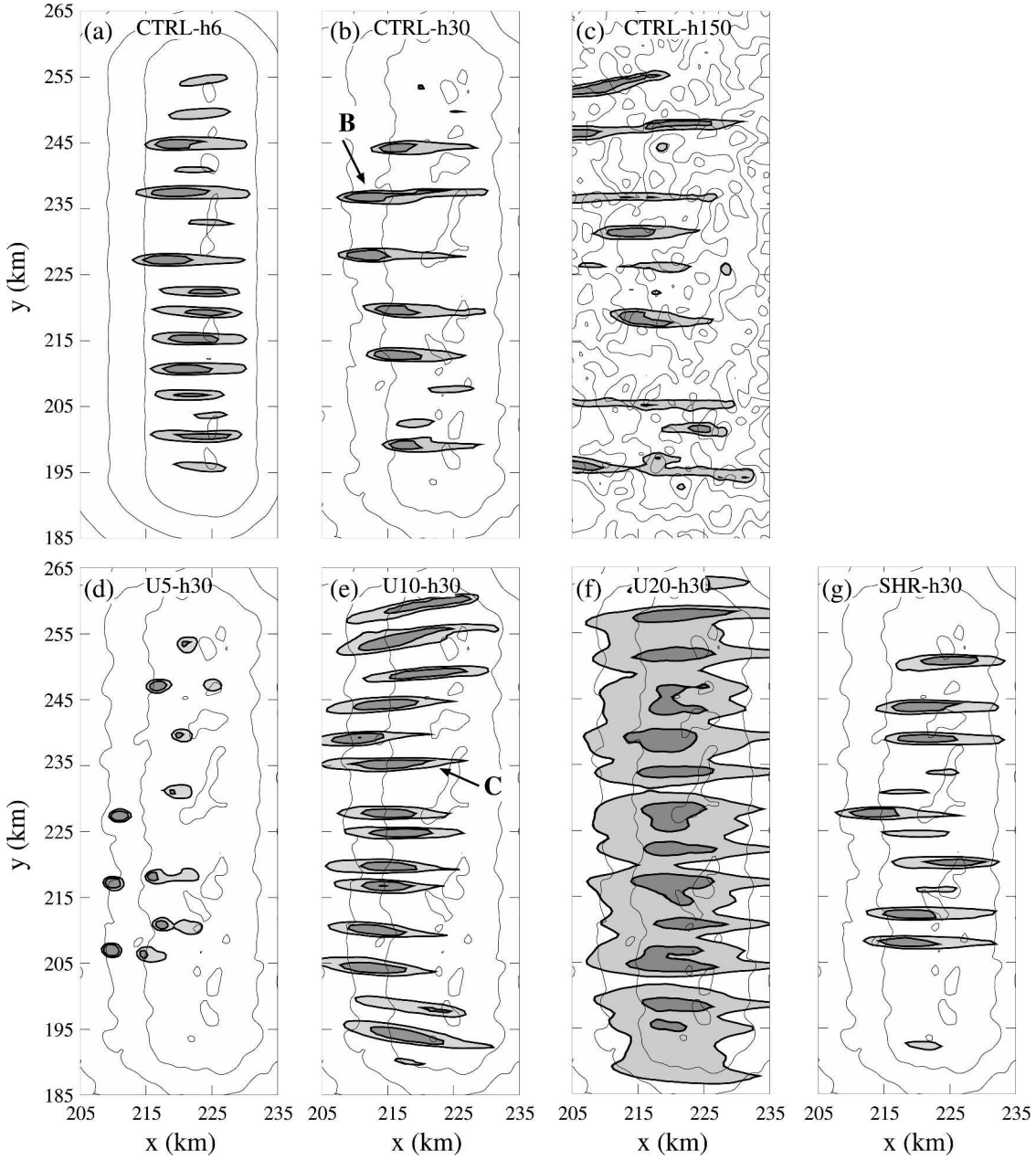

FIG. 4. As in Fig. 3, but for simulations with 30-m-rms small-scale topographic initiation: (a) CTRL-h6, (b) CTRL-h30, (c) CTRL-h150, (d) U5-h30, (e) U10-h30, (f) U20-h30, and (g) SHR-h30.

leading to a spatially variable precipitation distribution with large localized accumulations (Fig. 6c).

b. Sensitivity to perturbation amplitude

The choices of thermal and topographic perturbation amplitudes in the control simulations are arbitrary, and a range of amplitudes may be expected to occur. Mountain ranges are characterized by different levels of ruggedness, and the strength of thermal inhomogeneities depends on factors such as cloud cover, surface moisture availability, and the thermodynamic structure of the atmosphere. In particular, turbulent eddies in unstable planetary boundary layers may create strong thermal variations over small spatial scales. Fuhrer and Schär (2005) investigated the effects of thermal fluctuation amplitude on cellular orographic convection and found that higher-amplitude seeding led to more intense convection and heavier rainfall enhancements.

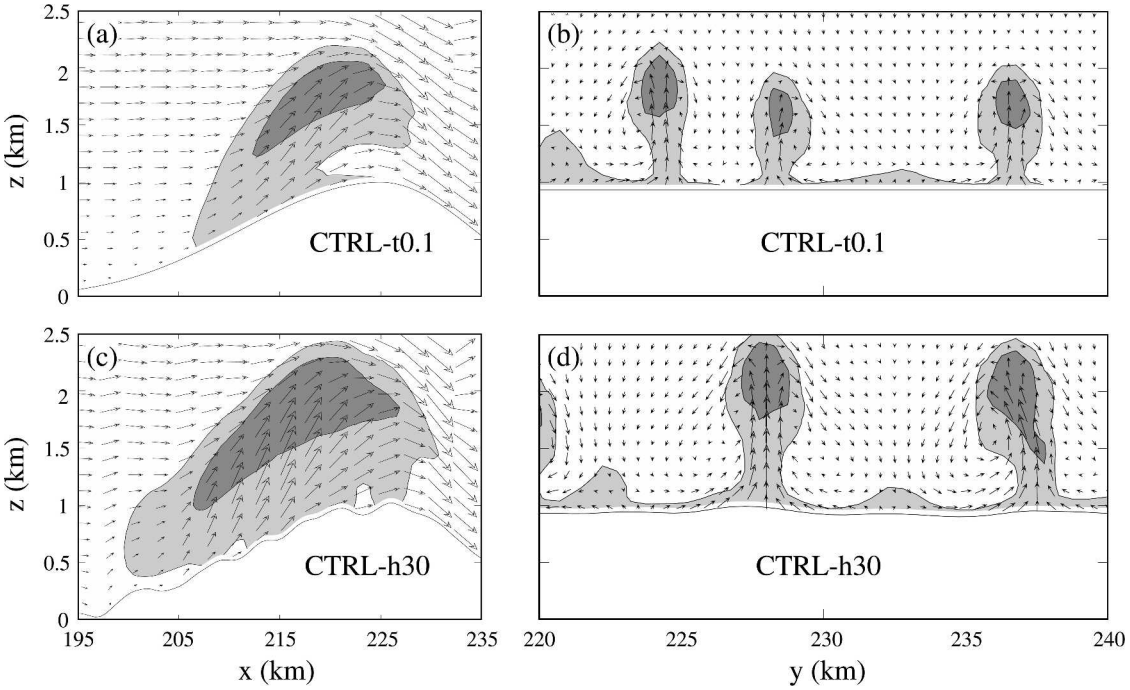

FIG. 5. Vertical cross sections of q_c and velocity vectors at $t = 3$ h, indicating roll-like convective circulations. Cross sections in the x–z plane of the (a) CTRL-t0.1 simulation at $y = 224$ km and (c) CTRL-h30 simulation at $y = 237$ km. Velocity vectors represent u and w components in plane parallel to cross section, and are plotted every vertical grid point and every fifth horizontal grid point. Cross sections in y–z plane at $x = 220$ km of the (b) CTRL-t0.1 and (d) CTRL-h30 simulations. Velocity vectors represent v and w components in plane parallel to cross section, and are plotted at all grid points. Shaded contours display q_c contours of 2 and 8×10^{-4} kg kg^{-1}.

The effect of the amplitude of the small-scale forcing on the bandedness of orographic convection has, however, not been previously determined. This is evaluated here through pairs of simulations in which the rms amplitudes of the initial perturbations are increased or decreased by a factor of 5 from those in the control simulations. These simulations include two cases with background thermal fluctuations possessing rms amplitudes of 0.02 and 0.5 K (CTRL-t0.02 and CTRL-t0.5) and two simulations with roughened topography possessing rms amplitudes of 6 and 150 m (CTRL-h6 and CTRL-h150).

The q_c fields shown at $z = 1.5$ km and $t = 3$ h in Figs. 3a–c and Figs. 4a–c demonstrate that the bandedness of orographic convection is considerably more sensitive to the strength of the background thermal noise than to the amplitude of the topographic roughness. This is most apparent in the cases where the perturbation amplitude is increased fivefold. The well-defined bands in the CTRL-t0.1 simulation (Fig. 3b) are severely degraded in the CTRL-t0.5 case (Fig. 3c), which produces more cellular and disorganized features. In the CTRL-h150 case (Fig. 4c), however, bands form that tend to be even longer and more stationary than those in the CTRL-h30 case (Fig. 4b), though they possess more finescale structure. By contrast, when the perturbation amplitude is reduced by a factor of 5, the responses to the two types of initial perturbations are similar. Both the thermally perturbed CTRL-t0.02 (Fig. 3a) and the topographically roughened CTRL-h6 (Fig. 4a) simulations produce convective bands that are shorter and more closely spaced than the respective reference cases (CTRL-t0.1 and CTRL-h30). As the perturbation amplitude is decreased by another factor of 5 (not shown), thermally initiated convection is inhibited completely, while topographic initiation still produces bands, although they are weaker and even shorter than those in Fig. 4a. Thus, it appears that a broader range of topographic roughness amplitudes, relative to those of the background thermal fluctuations, may be expected to lead to rainband formation.

4. Atmospheric parameters influencing bandedness

The thermodynamic and velocity profiles of the upstream sounding strongly influence the orographic flow on multiple scales. On the larger scale, whether the impinging flow travels over the mountain (unblocked flow) or detours around the mountain (blocked flow)

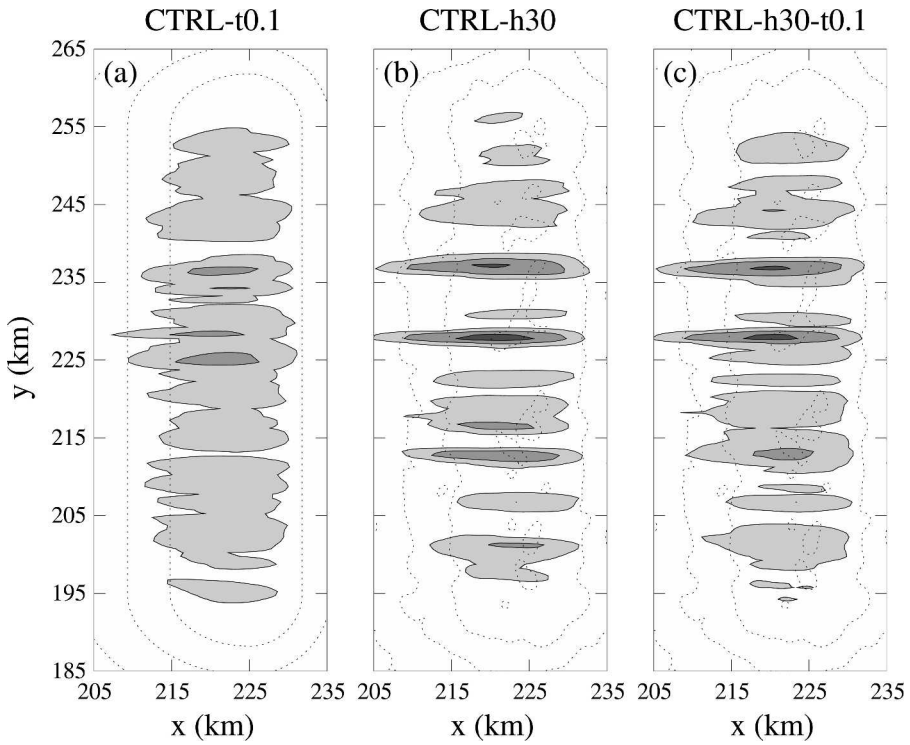

FIG. 6. Cumulative surface precipitation (P) fields of simuations at $t = 4$ h: (a) CTRL-t0.1, (b) CTRL-h30, and (c) CTRL-h30-t0.1. Shaded contours of P are 1, 5, and 15 mm. Topographic contours are shown by dashed lines at 250-m intervals.

has been shown to depend on the nonlinearity parameter $\epsilon = Nh/U$, where N and U are representative values for the Brunt–Väisälä frequency and cross-mountain wind speed of the low-level flow (e.g., Smith 1988). Given that ϵ is sufficiently small for air to ascend the mountain and form a cap cloud, the primary factors governing the submountain-scale convective structures that form within these clouds appear to be the low-level wind speed, vertical shear, and static stability. The simulations discussed in the following show the effects of these parameters on the bandedness of shallow orographic convection. Unless specified otherwise, the q_c plots for these cases are displayed in horizontal cross sections over the mountain at $z = 1.5$ km and $t = 3$ h.

a. Wind speed

Both the mountain wave–induced circulations that form the parent orographic cloud and the convective excitation provided within that cloud by small-scale topographic features are influenced by the wind speed. When the flow is strong enough and the static stability weak enough that the flow ascends the mountain rather than detouring laterally around it, stronger winds increase the vertical wavelength of the orographic wave pattern, resulting in a deeper orographic cap cloud, and they also reduce the residence time of air parcels in the unstable cloud region. Cloud depth and residence time were both found by Kirshbaum and Durran (2004) to influence the intensity of orographic convection. While deeper unstable clouds had higher perturbation growth rates, reduced residence times inhibited convection by limiting the time over which unstable perturbations were amplified within the cloud. In addition, the wind speed affects the flow response to submountain-scale topographic features that may initiate convection.

The effect of wind speed on both thermally and topographically initiated convection is investigated by comparing simulations identical to the control cases except that the vertical shear is removed and U is assigned a value that is uniform with height. Three different cases are considered: $U = 5$ m s^{-1} (U5-t0.1 and U5-h30), $U = 10$ m s^{-1} (U10-t0.1 and U10-h30), and $U = 20$ m s^{-1} (U20-t0.1 and U20-h30). Linear theory suggests that as U increases, the vertical wavelength of the mountain wave ($2\pi U/N$) also increases. For the ridge profile used in these simulations, the maximum wave-induced upward displacements over the windward slope occur at the surface and decrease with height until the level $z = \pi U/N$ is reached. Thus, the increase in vertical wavelength associated with increased U creates

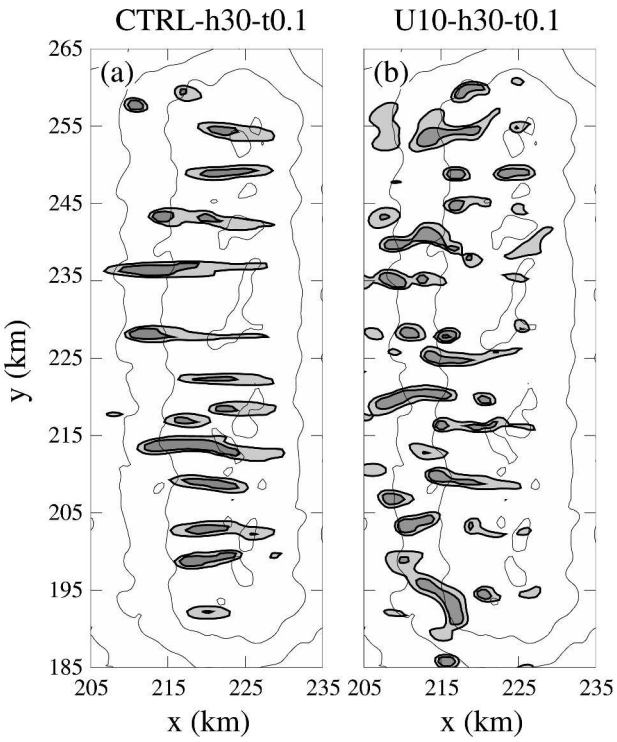

FIG. 7. Cloud liquid water (q_c) field of the (a) CTRL-h30-t0.1 and (b) U10-h30-t0.1 simulations. Contours of q_c are 4 and 8 $\times$ 10^{-4} kg kg^{-1}. Topographic contour interval is 250 m.

larger vertical displacements at low levels directly over the mountain. This is reflected by the q_c comparisons at $z = 1.5$ km in Figs. 3d–f and 4d–f in which the liquid water concentrations become progressively higher as the value of U is increased. The structure of orographic convection also depends strongly on U, particularly in the topographically roughened simulations, in which the wind speed controls the amplitude of the perturbations generated by flow over the roughened topography. While convection in the U5-h30 simulation is cellular and disorganized (Fig. 4d), well-defined and stationary bands form in the U10-h30 simulation (Fig. 4e), and weaker and more diffuse banded formations develop in the U20-h30 simulation (Fig. 4f). Thus, for intermediate values of U, well-defined bands appear to form over roughened topography even in the absence of basic-state vertical shear.

The quasi-stationary bands in the U10-h30 case appear to be triggered by lee waves induced by submountain-scale roughness elements upstream of the orographic cloud. This can be seen from the vertical cross sections in Fig. 8, which show shaded contours of positive vertical velocity at $t = 3$ h and $y = 235$ km of the U10-h30 simulation (along the center of band C in Fig. 4e) and a simulation that is identical except for the absence of moisture (U10-h30-dry). Unlike the U10-h30 simulation, which develops a statically unstable orographic cloud, the cloud-free U10-h30-dry simulation is statically stable at all locations. Several upstream-tilting, vertically coherent updrafts, labeled U1–U4 in Fig. 8, are present in both the moist and dry cases and are indicative of lee waves produced by stably stratified flow over the hilly underlying topography. Note that the amplitudes of the waves, particularly U3 and U4 over the mountain, are reduced in the U10-h30 case relative to those in the dry case because the statically unstable orographic cloud does not support lee waves.

The connection between lee waves and moist convection is evident at $x \approx 195$ km in Fig. 8a, where the lee wave updraft U2 intersects the leading edge of the potentially unstable cap cloud. Lee wave updrafts similar to U2 are present at the upstream edges of all the convective bands in the U10-h30 case, suggesting that these perturbations act to trigger the moist convection. The underlying small-scale topographic features that induce these lee waves are optimally positioned when they are just upstream of the orographic cloud so that the waves form in an essentially stable flow but still extend into the unstable cloud region.

In contrast to the sometimes-banded convective response over roughened topography, orographic convection initiated purely by background thermal noise never organizes into bands in those simulations without basic-state vertical shear. This is seen by the cellular features in both the U5-t0.1 (Fig. 3d) and U10-t0.1 (Fig. 3e) simulations and the irregular pattern of cloudiness that develops in the U20-t0.1 simulation (Fig. 3f). Without sufficient vertical wind shear, no mechanism exists to break the local isotropy of the convection over a smooth mountain, regardless of the strength of the wind. A small amount of vertical shear does develop in these flows as a result of upstream blocking and vertically propagating gravity waves, but the total increase in the westerly wind with height over the lowest 3 km at the upstream edge of the windward slope ($x = 205$ km) is much larger in the control cases (0.004 s^{-1}) than in any of the constant wind speed cases (0.001 s^{-1}). Furthermore, in the control case, the vertical shear maintains its strength from the windward slope all the way past the mountain crest, but it drops to almost zero halfway up the mountain slope in the constant wind speed cases. The disorganized patterns of convection in the U5-t0.1, U10-t0.1, and U20-t0.1 simulations (Figs. 3d–f) suggest that this weak orographically induced shear is insufficient to single-handedly organize the convection into bands.

Although the upstream wind speed does not always

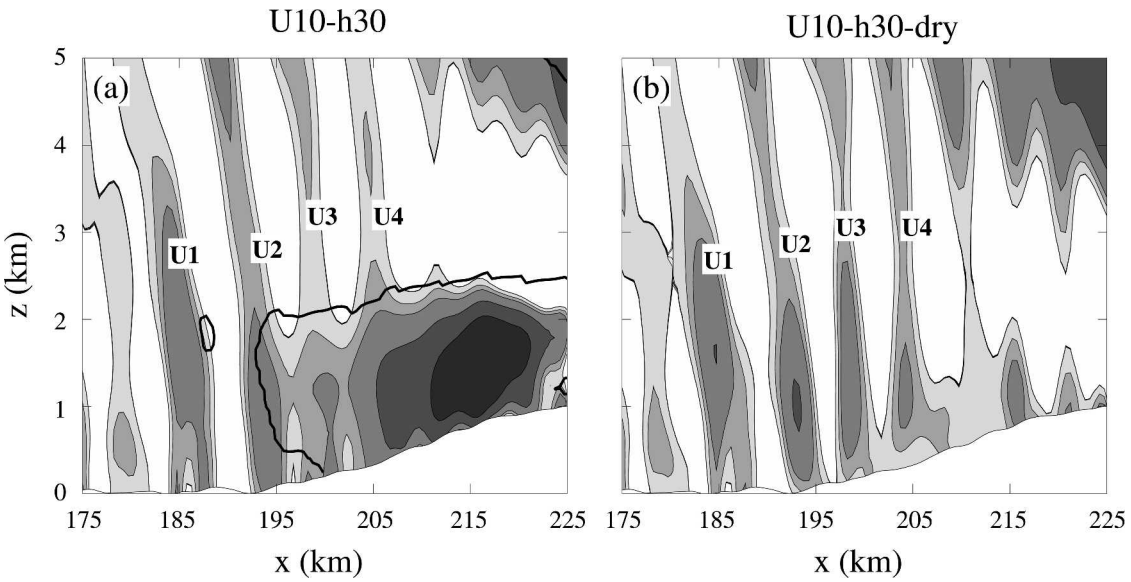

FIG. 8. Positive vertical velocity (w) fields of x–z cross sections of the (a) U10-h30 and (b) U10-h30 dry simulations at $y = 235$ km. Contours of w are 0, 0.1, 0.2, 0.5, 1, and 2 m s^{-1}. Cloud outline, given by 1×10^{-6} kg kg^{-1} contour, is plotted in (a).

govern the organization of orographic convection, it influences the depth of the cap cloud (through changes in the vertical wavelength of the mountain wave) and the in-cloud residence time of unstable perturbations and, thus, influences the convective intensity. For example, as U is increased from 10 m s^{-1} in the U10-t0.1 and U10-h30 simulations to 20 m s^{-1} in the U20-t0.1 and U20-h30 simulations, the residence time is roughly halved while the cloud is deepened. Most of the increased cloud volume in the stronger-wind cases, however, lies in the layer above $z = 2.5$ km and is statically stable, so the growth rates of the convective perturbations are not strongly affected by the increased cloud depth. As a result, the reduced residence times directly inhibit the development of convection inside the unstable portion of the orographic cloud, which can be seen by the weak convective structures in the $U = 20$ m s^{-1} cases (Figs. 3f and 4f) relative to the $U = 10$ m s^{-1} cases (Figs. 3e and 4e).

As in the CTRL-h30-t0.1 simulation in Fig. 7a, the q_c field of an additional simulation (U10-h30-t0.1) with $U = 10$ m s^{-1} and combined thermal and topographic excitation shown in Fig. 7b indicates a mixture of the separate convective responses to each of the perturbation types. However, unlike the CTRL-h30-t0.1 case in which both initiation mechanisms produced qualitatively similar bands that reinforced each other, the cellular features initiated by background thermal fluctuations in the U10-h30-t0.1 case disrupt the bands that form over roughened topography, leading to a less organized and stationary pattern. The different convective responses to the different methods of small-scale initiation in the U10-t0.1, U10-h30, and U10-h30-t0.1 simulations are reflected in the cumulative precipitation fields in Fig. 9. While the transient cells in the U10-t0.1 simulation distribute relatively light precipitation evenly over the mountain (Fig. 9a) with a modest maximum accumulation (21 mm), the quasi-stationary bands in the U10-h30 simulation generate a more banded precipitation field (Fig. 9b) with much larger localized accumulations and a higher maximum (55 mm). Despite its increased overall excitation, the lack of organized, quasi-stationary bands in the U10-h30-t0.1 simulation results in a less banded precipitation field (Fig. 9c) with a much lower maximum accumulation (31 mm) than the U10-h30 case.

b. Vertical shear

The presence of convective bands in the thermally perturbed CTRL-t0.1 simulation, and their absence in the unsheared thermally perturbed simulations of section 4b (U5-t0.1, U10-t0.1, and U20-t0.1), suggest that vertical shear plays an important role in organizing orographic convection. This may be explained by the tendency for convection to form into bands aligned with the shear vector in statically unstable shear flows. Shear-parallel roll circulations were found to be the preferred mode of convection for small-amplitude perturbations in numerous linear stability analyses, among them Kuo (1963) and Asai (1970). A physical explana-

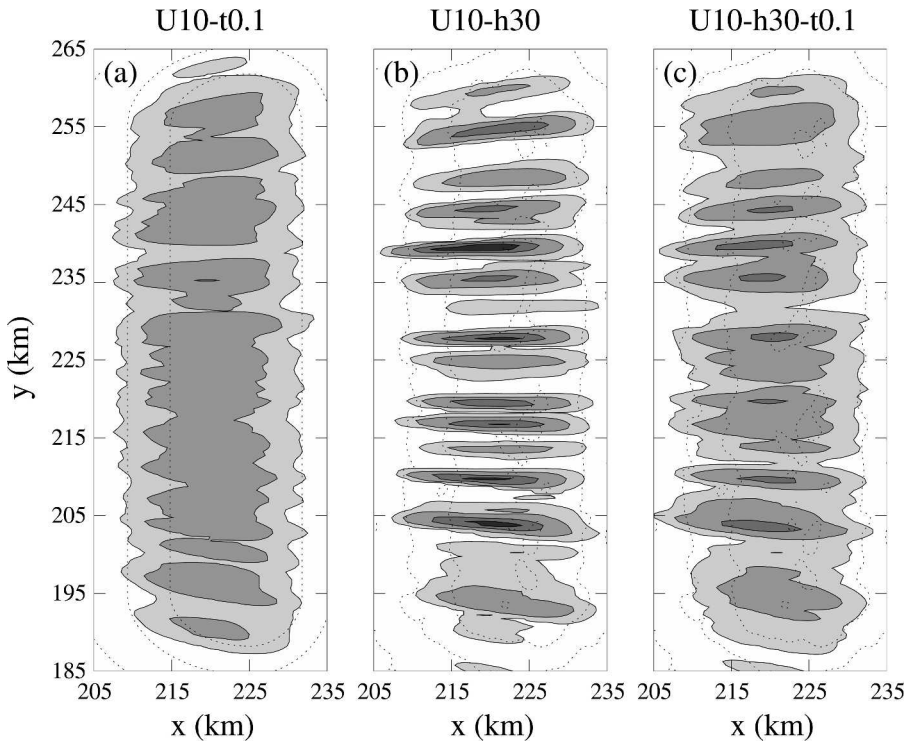

FIG. 9. Cumulative surface precipitation (P) fields of simuations of $t = 4$ h: (a) U10-t0.1, (b) U10-h30, and (c) U10-h30-t0.1. Shaded contours of P are 1, 5, 20, and 40 mm. Topographic contours are shown by dashed lines at 250-m intervals.

tion for this behavior was provided by Asai (1964), who numerically solved the linear Boussinesq set of equations for a two-dimensional statically unstable shear flow describing cross-shear convective circulations. It was found that the phase coherence of convective velocity and temperature perturbations is disrupted by vertical shear, which inhibits the conversion of available potential energy into perturbation kinetic energy. Moreover, the downshear tilt of the convective axis causes upward momentum transport, which reduces the strength of the unstable perturbations by converting perturbation kinetic energy into that of the mean flow. Elongated convective rolls with axes parallel to the shear are not adversely influenced by these processes, so they have comparatively fast growth rates and are favored to develop in flows with sufficient amounts of shear.

The influence of vertical shear on orographic convection is demonstrated by two pairs of simulations that are identical to the control simulations except that the vertical shear over the $0 \leq z \leq 5$ km layer is completely removed in the first set (U5-t0.1 and U5-h30, previously discussed in section 4a) and increased by a factor of 2 in the second set (SHR-t0.1 and SHR-h30) in which U increases linearly from 5 m s^{-1} at the surface to 35 m s^{-1} at $z = 5$ km and remains constant farther aloft. Unlike the well-defined bands in the CTRL-t0.1 simulation (Fig. 3b), convection takes the form of disorganized and randomly distributed cells when shear is removed in the U5-t0.1 simulation (Fig. 3d). The increased shear in the SHR-t0.1 simulation (Fig. 3g) yields results similar to the CTRL-t0.1 case except that the bands are shorter, form farther downstream, and have decreased spacing between them. These results suggest that a certain amount of shear is necessary to organize orographic convection into well-defined bands, beyond which the reduced residence times of air parcels in the orographic cloud may limit the strength of the convection and push it farther downstream. Similar behavior is evident for the topographically initiated convection in the U5-h30 (Fig. 4d), CTRL-h30 (Fig. 4b), and SHR-h30 (Fig. 4g) simulations, except that the reduction in band length associated with increased shear is not as prominent between the CTRL-h30 to SHR-h30 cases.

In all of the vertically sheared flows considered thus far, the mean wind and shear vectors spanning the cloud layer have been parallel. To distinguish between

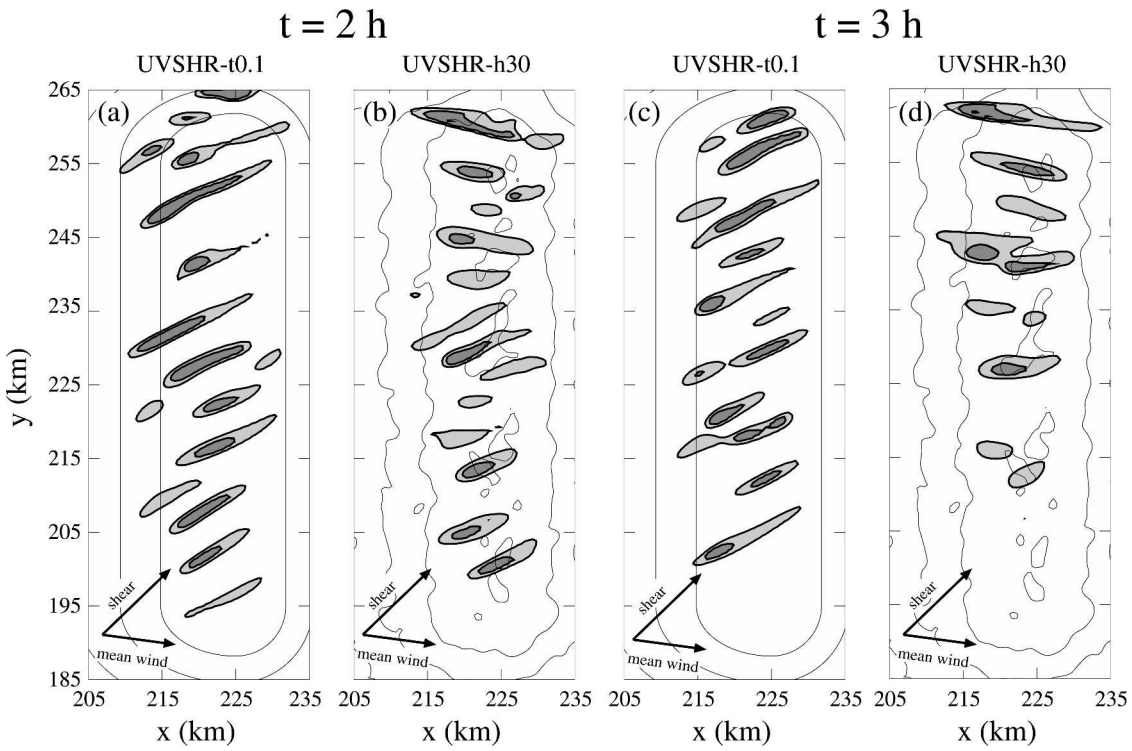

FIG. 10. Cloud liquid water (q_c) fields at $z = 1.5$ km and $t = 3$ h of directionally sheared simulations: (a) UVSHR-t0.1 and (b) UVSHR-h30 at $t = 2$ h; (c)–(d) as in (a)–(b), but at $t = 3$ h. Basic-state vertical shear and mean wind vector directions over $0 \leq z \leq 2.5$ km shown by arrows overlaid in (a)–(d). Topographic contour interval is 250 m.

the effects of the shear and the mean wind, these two vectors are separated by approximately 60° in two simulations (UVSHR-t0.1 and UVSHR-h30) that are identical to the CTRL-t0.1 and CTRL-h30 simulations except for the addition of a basic-state y velocity component (V) that increases from -5 m s^{-1} at the surface to 10 m s^{-1} at $z = 5$ km (the same amount of shear as in the x direction). As in the CTRL-0.1 case (Fig. 3b), the cloud field of the UVSHR-t0.1 simulation, shown at both $t = 2$ h (Fig. 10a) and $t = 3$ h (Fig. 10c), is organized into well-defined convective bands, but these bands are now oriented at 30°–40° counterclockwise from the horizontal, roughly parallel to the shear vector. In this case, directional vertical shear appears to effectively organize the thermally initiated convection into shear-parallel bands.

In contrast, the organization of convection over roughened topography is reduced when the basic-state wind turns with height, as the q_c field of the UVSHR-h30 simulation at $t = 2$ h (Fig. 10b) indicates weaker bands that appear to have multiple alignments. Some of these bands are roughly parallel to the mean wind over the cloud layer ($0 \leq z \leq 2.5$ km), while other elongated formations are oriented SW–NE like the shear-parallel bands in the UVSHR-t0.1 simulation. The coexistence of convective bands with different orientations in the UVSHR-h30 simulation suggests that roughened topography triggers bands with two different modes of organization: quasi-stationary flow-parallel bands linked to small-scale surface features like those in the U10-h30 simulation and propagating shear-parallel formations like the bands in the UVSHR-t0.1 simulation. As the mesoscale flow becomes steadier at $t = 3$ h, the transient fluctuations shed by the bumpy topography become very weak and, as a consequence, the shear-parallel bands vanish (Fig. 10d). Convection at this time consists of a few quasi-stationary flow-parallel bands and some other disorganized features. The overall convective pattern resulting from this competition between the two modes is weaker and less organized, suggesting that well-defined convective bands initiated by small-scale topographic roughness are most effectively generated in flows without strong directional shear.

The influence of directional wind shear may also explain the along-ridge variation in the UVSHR-h30 simulation (Figs. 10b and 10d) in which flow-parallel bands form on the northern half of the ridge and shear-parallel bands (or no convection at all) form(s) to the south. Unlike the pure westerly flow simulations previously discussed, in which the orographically induced

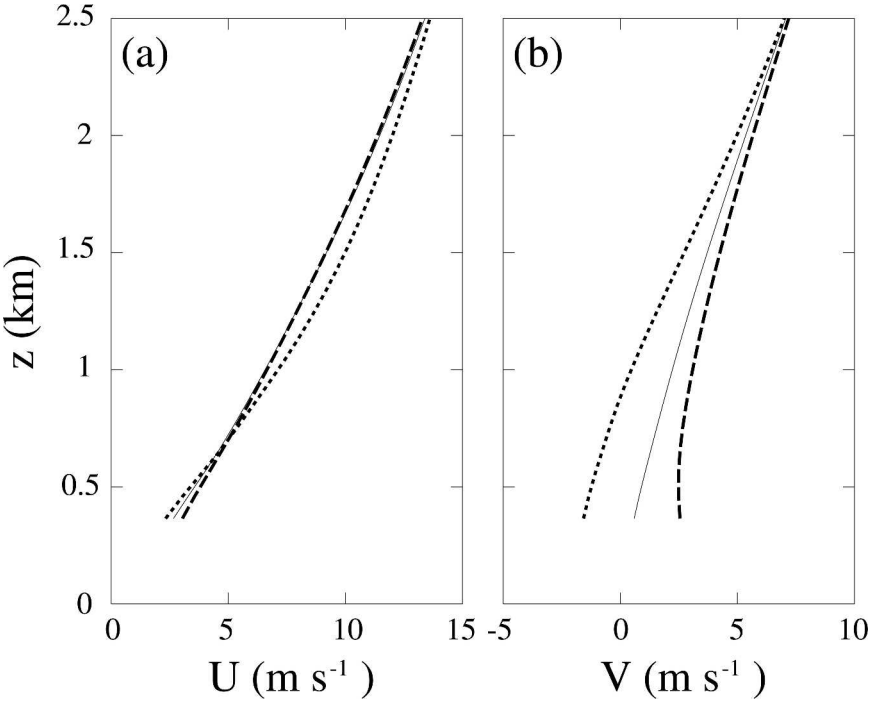

FIG. 11. Vertical profiles of (a) u and (b) v of the UVSHR-dp simulation upstream of the mountain crest at $x = 205$ km, $t = 2$ h, and three different values of y. The thick dotted line corresponds to $y = 200$ km, the thin solid line corresponds to $y = 225$ km, and the thick dashed line corresponds to $y = 250$ km.

shear was roughly parallel to the flow direction and uniform in the N–S direction along the windward slope (not shown), upstream blocking effects in this case strongly affect the amount of *directional* shear at different N–S locations along the upslope. This is seen by comparing vertical profiles of the full horizontal velocities u and v at a fixed x location (205 km) and three different y locations (200, 225, and 250 km) of a third directional-shear simulation (UVSHR-dp) at $t = 2$ h in Fig. 11. This simulation is identical to the UVSHR-t0.1 and UVSHR-h30 cases except that it is performed in double precision (to limit numerical roundoff error) and free of any small-scale thermal or topographic perturbations that might initiate convection. Thus it provides a clean depiction of the background state in which convection develops. Like the westerly flow cases considered earlier, the vertical shear in u (Fig. 11a) does not vary significantly along the ridge axis. However, considerable N–S differences now exist in the v shear (Fig. 11b). The near-surface flow is deflected to the south at $y = 200$ km, enhancing the directional shear at the southern end of the ridge, while the flow is deflected to the north and the directional shear is weakened at the ridge's northern end ($y = 250$ km). The stronger directional shear over the southern half of the mountain appears to suppress the flow-parallel mode, while the relatively weak directional shear on the northern end of the ridge allows this mode to prevail.

c. Stability

In addition to vertical shear, the degree of low-level static stability may influence the bandedness of shallow orographic convection. This is suggested by the linear stability analysis of Kuo (1963), who found that the organization of dry convection in a parallel shear flow depends on the Richardson number (Ri), given by the ratio of the static stability (N^2) to the square of the vertical shear ($[dU/dz]^2 + [dV/dz]^2$) in the unstable layer. In flows that are sufficiently unstable for perturbations to overcome diffusional effects, shear-parallel rolls have much faster growth rates than modes with other orientations when Ri is just slightly negative (indicative of relatively strong shear and weak instability). As Ri becomes more negative, the growth rates of other convective modes become comparable to that of shear-parallel rolls, leading to a more disorganized overall convective pattern. Observational studies of boundary layer convection support Kuo's findings; for example, Woodcock (1940) determined that linear patterns of motion, representative of roll vortices in that layer, only occurred for a narrow range of slightly negative Ri. Weak static instability and strong shear were

also associated with more roll-like boundary layer convection by Grossman (1982) and Weckwerth et al. (1997).

It is unclear to what extent the theory for dry convection over flat terrain applies to unstable orographic clouds. Aside from the use of a different stability parameter (the moist Brunt–Väisälä frequency N_m^2 rather than N^2), *small amplitude* motions within clouds are governed by the same dynamics as those in unsaturated layers (e.g., Durran and Klemp 1982). For larger amplitude displacements in which the downdrafts become unsaturated, nonlinearities introduced by the difference in stability between clear and cloudy regions makes the moist problem far more complex. Orographic clouds are complicated even further by the fact that they form over sloping terrain and have limited spatial extent.

The effect of atmospheric stability on banded orographic convection is investigated by comparing the vertically sheared CTRL-t0.1 and CTRL-h30 simulations with three pairs of simulations that are identical except for different values of N_1 and T_s, which produce different combinations of dry stability and in-cloud moist stability. Dry stabilities are specified by the value of N_1, which also affects the in-cloud moist-stability through its influence on the temperature lapse rate. For a given value of N_1, the static stability within the cloud is also dependent on T_s because, like the moist-adiabatic lapse rate, N_m^2 decreases as the temperature increases. In the remainder of this section, the simulations are identified according to their values of T_s, N_1, and the method used to initialize the small-scale perturbations. Thus, the CTRL-t0.1 and CTRL-h30 simulations will now be referred to as the T285-N01-t0.1 and T285-N01-h30 simulations. In the other cases, N_1 and T_s are decreased to 278 K and 0.0085 s^{-1} in the T278-N0085 sounding, T_s is increased to 295 K in the T295-N01 sounding, and N_1 is decreased to 0.0085 s^{-1} in the T285-N0085 sounding. The θ_e profiles of these four soundings are compared in Fig. 2, indicating that the T278-N0085 and T285-N01 soundings exhibit marginal potential instability over $0 \leq z \leq 2.5$ km, while the T295-N01 and T285-N0085 soundings have much greater potential instability over the same layer.

The nominal in-cloud moist stabilities of the various simulations described above are quantitatively compared by the N_m^2 fields at $t = 1$ h in Figs. 12a–d. The laminar clouds in these plots, which indicate the background state in the absence of convection, are produced by four 2D simulations using the soundings just described (T285-N01–2D, T278-N0085–2D, . . .). These 2D simulations are identical in computational design to the 3D simulations described previously except that the numerical domain is collapsed to a single x–z plane along the centerline of the mountain and, as in the UVSHR-dp simulation, the calculations are performed in double precision (to limit numerical roundoff error) without any small-scale perturbations that might initiate convection within the cloud. All of the laminar clouds in Fig. 12 are statically unstable, with the more negative N_m^2 values indicative of more instability. The T285-N0085–2D and T295-N01–2D simulations produce cap clouds with similar values of N_m^2 (Figs. 12b and 12d) that are more negative than the T285-N01–2D case (Fig. 12a), indicating greater moist instability. The combination of reduced temperature and background (dry) stability in the T278-N0085–2D simulation (Fig. 12b) produces a cloud with weak moist instability like that in the T285-N01–2D case.

In the presence of background thermal inhomogeneities, these different thermodynamic profiles produce varying levels of bandedness in the 3D simulations. Comparing the q_c fields of the T285-N01-t0.1 (Fig. 12e) and T295-N01-t0.1 (Fig. 12f) simulations, which have the same dry stabilities, the bands are clearly more elongated and better organized in the case with the cooler temperatures. When the temperatures are warmer, the moist instability within the cap cloud is stronger, producing a less organized mixture of bands and cells. Similarly, although both cases have the same dry stability, convection in the more moist unstable T285-N0085-t0.1 simulation (Fig. 12d) is slightly more cellular than that in the T278-N0085-t0.1 simulation (Fig. 12c). These results suggest that, for a given value of background dry stability, weaker levels of in-cloud moist instability favor more banded orographic convection.

The bandedness of thermally initiated convection appears to depend just as strongly on the dry stability of the surrounding environment, which influences the subsiding branches of the convective circulations. Comparing the q_c fields of the T285-N01-t0.1 (Fig. 12e) and T278-N0085-t0.1 simulations (Fig. 12g), which have nearly identical moist instabilities, the convection in the case with stronger dry stability is clearly more banded. Likewise, in spite of their similar moist stabilities, the T295-N01-t0.1 simulation (Fig. 12f) is more banded than the T285-N0085-t0.1 case (Fig. 12h). These results suggest that both the in-cloud moist stability and the dry stability of the surrounding environment influence the bandedness of the convection. The combination of weakly unstable clouds and a strongly stable surrounding environment, such as that in the T285-N01-t0.1 simulation, appears to be the most favorable for organized bands. This combination of factors produces convective circulations with relatively slow growth rates,

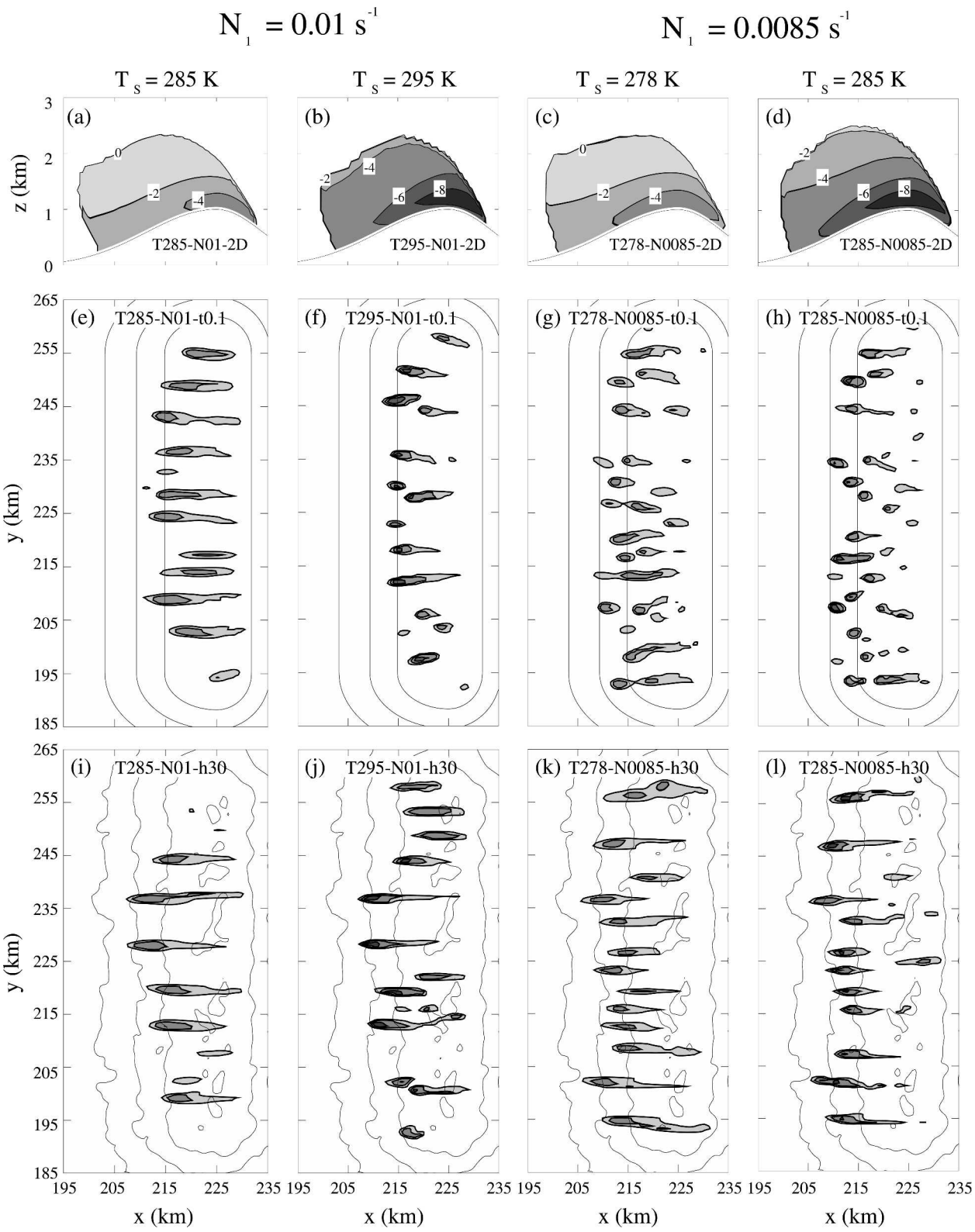

FIG. 12. Comparison of simulations with different values of T_s and N_1. Moist Brunt–Väisälä frequency (N_m^2) fields of double precision: (a) T285-N01–2D, (b) T295-N01–2D, (c) T278-N0085–2D, and (d) T285-N0085–2D. Cloud liquid water (q_c) fields at $z = 1.5$ km and $t = 3$ h of the (e) T285-N01-t0.1, (f) T295-N01-t0.1, (g) T278-N0085-t0.1, and (h) T285-N0085-t0.1 simulations. (i)–(1) As in (e)–(h), but for T285-N01-h30, T295-N01-h30, T278-N0085-h30, and T285-N0085-h30. Contours of N_m^2 in (a)–(d) are multiplied by 10^{-5} s^{-2}; contours of q_c in (e)–(i) are 4, 8, and 12×10^{-4} kg kg^{-1}.

which allows the shear to more effectively organize the convection into rolls before the moist instability is released.

Comparing the q_c fields of the topographically roughened simulations (Figs. 12i–l) with the thermally perturbed cases (Figs. 12e–h), the overall convective patterns are clearly more banded over roughened topography. Nonetheless, the elongation and organization of the topographically initiated convection still exhibits some dependence on the moist and dry stabilities. Convective bands are the most elongated and evenly spaced in the T285-N01-h30 case (Fig. 12i) and become less organized as the moist instability is increased in the T295-N01-h30 (Fig. 12j), or the dry stability is decreased (with no accompanying changes in the moist stability) in the T278-N0085-h30 case (Fig. 12k). As in the simulations with thermal initiation, the shortest bands develop in the case with the weakest dry stability and strongest moist instability (T285-N0085-h30 in Fig. 12l).

5. Conclusions

Recent observations suggest that quasi-stationary rainbands may be a common form of shallow orographic convection that is capable of causing localized heavy precipitation. To determine the environmental conditions favoring the formation of these rainbands, this study has investigated, through numerical simulation, the convective responses of unstable orographic clouds to different atmospheric factors and initiation mechanisms. The simulations used a simplified topographic profile representing a section of the Oregon Coastal Range and a reference sounding based on cases of banded orographic convection that have been observed over this regions. The upstream soundings were varied to determine the effects of wind speed, vertical shear, and stability on the structure of orographic convection.

Two different small-scale mechanisms by which orographic rainbands were initiated in the numerical simulations are thermal inhomogeneities carried with the flow and roughness elements added to the mountainous topography. In flows with unidirectional vertical shear and marginally unstable orographic cap clouds, both initiation types generated well-defined flow-parallel rainbands. These bands were found in the updrafts of roll-like convective circulations with unsaturated areas in the downdrafts. Apart from small differences in the efficiency with which they excited convection, the main difference between the these two initiation mechanisms was the stationarity of the bands they produced. Random thermal perturbations embedded in the flow triggered transient bands that distributed rainfall evenly over the mountain, whereas small-scale topographic bumps generated quasi-stationary bands, focusing precipitation over preferred areas. Large localized precipitation accumulations thus are more likely to be produced by steady convective bands forced by small-scale topographic features rather than the transient bands initiated by small-scale fluctuations in the background flow.

Over smooth orography, the convection initiated by embedded thermal perturbations only organized into bands in the presence of vertical shear. The shear appeared to suppress convective circulations with axes that were aligned nonparallel to the shear vector, thus favoring the development of elongated shear-parallel formations. The organization of these bands, which translated over the mountain with the prevailing flow, was maximized in flows with weakly unstable orographic clouds that were surrounded by strongly stable dry regions. This combination of stabilities was associated with the slowest convective growth rates and allowed the shear to most effectively organize the convection into bands.

Unlike the exclusively shear-parallel organization of convective bands initiated by background thermal noise, topographically initiated convection also possessed a flow-parallel mode that formed quasi-stationary bands even in the absence of shear (over a limited range of wind speeds). This more dominant quasi-stationary flow-parallel mode appeared to be triggered by lee waves formed by statically stable flow over small-scale topographic features just upstream of the orographic cloud. The precise dynamics by which these well-defined and stationary bands are triggered by small-scale topography is a subject of ongoing investigation that will be addressed in a subsequent paper.

The quasi-stationary bands triggered by lee waves over roughened topography were considerably more robust than the transient shear-parallel bands initiated by embedded thermal perturbations. These rainbands formed over a wider range of perturbation amplitudes and exhibited less sensitivity to the strength of the vertical shear and the low-level static stability. The organization of bands generated by topographic roughness was, however, degraded by directional shear because, as the wind direction turned with height, the vertical shear tended to suppress the flow-parallel bands and generate a secondary shear-parallel mode.

In real-world flows, which contain some mixture of background thermal fluctuations and topographic roughness, favorable conditions for bands include 1) weak moist instability (or potential instability) and strong dry stability in the lower-tropospheric layer that is eventually lifted to saturation over the mountain and

2) a strongly sheared wind profile that is almost unidirectional through the depth of the cloudy layer. Since operational weather forecasts generally lack the horizontal resolution necessary to capture small-scale convection like that simulated in this study, these guidelines might help to predict whether upstream flows impinging upon a mountain should be expected to produce quasi-stationary rainbands.

Acknowledgments. This material is based upon work supported by the National Science Foundation under Grants ATM-9979241 and ATM-0225441.

REFERENCES

Asai, T., 1964: Cumulus convection in the atmosphere with vertical wind shear: Numerical experiment. *J. Meteor. Soc. Japan,* **42,** 245–258.

——, 1970: Three-dimensional features of thermal convection in a plane couette flow. *J. Meteor. Soc. Japan,* **48,** 18–29.

Cosma, S., E. Richard, and F. Miniscloux, 2002: The role of small-scale orographic features in the spatial distribution of precipitation. *Quart. J. Roy. Meteor. Soc.,* **128,** 75–92.

Durran, D. R., and J. B. Klemp, 1982: On the effects of moisture on the Brunt–Väisälä frequency. *J. Atmos. Sci.,* **39,** 2152–2158.

——, and ——, 1983: A compressible model for the simulation of moist mountain waves. *Mon. Wea. Rev.,* **111,** 2341–2361.

Epifanio, C. C., and D. R. Durran, 2001: Three-dimensional effects in high-drag-state flows over long ridges. *J. Atmos. Sci.,* **58,** 1051–1065.

Fuhrer, O., and C. Schär, 2005: Embedded cellular convection in moist flow past topography. *J. Atmos. Sci.,* **62,** 2810–2828.

Grossman, R. L., 1982: An analysis of vertical velocity spectra obtained in the bomex fair-weather, trade-wind boundary layer. *Bound.-Layer Meteor.,* **23,** 323–357.

Kirshbaum, D. J., and D. R. Durran, 2004: Factors governing cellular convection in orographic precipitation. *J. Atmos. Sci.,* **61,** 682–698.

——, and ——, 2005: Observations and modeling of banded orographic convection. *J. Atmos. Sci.,* **62,** 1463–1479.

Kuo, H. L., 1963: Perturbations of plane couette flow in stratified fluid and origin of cloud streets. *Phys. Fluids,* **6,** 195–211.

Leveque, R. J., 1996: High-resolution conservative algorithms for advection in incompressible flow. *SIAM J. Numer. Anal.,* **33,** 627–665.

Lilly, D. K., 1962: On the numerical simulation of buoyant convection. *Tellus,* **14,** 148–172.

Miniscloux, F., J. D. Creutin, and S. Anquetin, 2001: Geostatistical analysis of orographic rainbands. *J. Appl. Meteor.,* **40,** 1835–1854.

Smith, R. B., 1988: Linear theory of stratified flow past an isolated mountain in isosteric coordinates. *J. Atmos. Sci.,* **45,** 3889–3896.

Weckwerth, T. M., J. W. Wilson, R. M. Wakimoto, and N. A. Crook, 1997: Horizontal convective rolls: Determining the environmental conditions supporting their existence and characteristics. *Mon. Wea. Rev.,* **125,** 505–526.

Woodcock, A. H., 1940: Convection and soaring over the open sea. *J. Mar. Res.,* **3,** 248–253.

Yoshizaki, M., T. Kato, Y. Tanaka, H. Takayama, Y. Shoji, and H. Seko, 2000: Analytical and numerical study of the 26 June 1998 orographic rainband observed in western Kyushu, Japan. *J. Meteor. Soc. Japan,* **78,** 835–856.